FINAL REPORT

Standardized Analysis for UXO Demonstration Sites

ESTCP Project MM-0413

APRIL 2008

Thomas Bell
AETC Incorporated

Approved for public release; distribution unlimited.

Environmental Security Technology Certification Program

Contents

Contents i
Figures ii
Tables ii
Acronyms iii
1. Introduction 1
1.1 Background 1
1.2 Technical Approach 1
2. Standardized Sites 3
2.1 Site Descriptions 3
2.2 Data Sets 3
3. EMI Data Analysis 10
3.1 Target Depth Estimation Results 12
3.2 Target Size Estimation Results 13
3.3 Target Shape Parameters 14
3.4 UXO/Clutter Discrimination 16
4. Magnetometer Data Analysis 18
4.1 Dipole Fit Quality and SNR 18
4.2 Target Size and Depth 19
4.3 Remnant Magnetization 21
5. Multiple Targets 22
6. Summary and Conclusions 23
7. References 24

Figures

Figure 1. Standardized UXO demonstration sites at Aberdeen Proving Ground (left) and Yuma Proving Ground (right). 4
Figure 2. NRL MTADS EM61 array (inset) and diagram of EMI field below the array. 6
Figure 3. EMI demonstration systems: (a) NAEVA Geophysics manportable EM61, (b) NAEVA Geophysics EM61 towed array, (c) TtFW EM61, (d) ERDC EM63. 7
Figure 4. NAEVA EM61 survey maps for YPG Blind Grid (left) and Open Field (right). 8
Figure 5. APG survey maps. ERDC EM63 survey of Blind Grid on the left, and NRL survey of the open field on the right. 8
Figure 6. Magnetometer surveys. (a) Shaw survey of APG Blind Grid, (b) MTADS survey of APG Open Field, (c) MTADS survey of YPG Open Field. 9
Figure 7. Shaw pushcart magnetometer system (left) and MTADS towed magnetometer array (right). 9
Figure 8. Comparison of EM63 inversion with principal axis angles fixed in time or variable. 10
Figure 9. Beta values for various UXO and clutter items. 11
Figure 10. Dipole fit quality *vs.* SNR for the TtFW EM61 data. 12
Figure 11. Target depth estimates (in meters) from TtFW EM61 survey data compared with ground truth depths. 12
Figure 12. Estimated depths from the different EMI surveys compared with ground truth depths. 13
Figure 13. Apparent target size from dipole fit *vs.* caliber for UXO targets. 14
Figure 14. UXO polarizabilities from TtFW EM61 survey data. 15
Figure 15. UXO polarizabilities from MTADS EM61array survey data. 15
Figure 16. UXO polarizabilities from ERDC and NAEVA survey data, fit quality > 0.99. 15
Figure 17. UXO and clutter betas from MTADS EM61 array survey data, fit quality > 0.99. 16
Figure 18. Dipole model fit error *vs.* target signal to noise ratio (SNR) for EM61 data collected in SERDP project MM-1310. 17
Figure 19. Magnetic dipole fit quality *vs.* SNR for Shaw pushcart and MTADS magnetometer array. 18
Figure 20. Comparison of MTADS and Shaw data for anomaly E07 in APG Blind Grid. 19
Figure 21. Target depth estimates from MTADS magnetometer array data compared with ground truth. 19
Figure 22. Comparison of estimated depths from MTADS and Shaw magnetometer data. 20
Figure 23. Dipole fit size estimates compared with ground truth for MTADS data (left) and comparison of Shaw and MTADS size estimates for common targets (right). 20
Figure 24. Comparison of dipole size estimates for degaussed and non-degaussed UXO targets. 21
Figure 25. Fit quality distributions for multiple (red) and single (black) targets. MTADS magnetometer array data on left, TtFW EM61 data on right. 22

Tables

Table 1. Data Sets Analyzed 4

Acronyms

AETC	AETC Incorporated
APG	Aberdeen Proving Ground
DGPS	Differential GPS
EMI	Electromagnetic Induction
ERDC	Environmental Research and Development Center
ESTCP	Environmental Security Technology Certification Program
GPS	Global Positioning System
MTADS	Multisensor Towed Array Detection System
NAEVA	NAEVA Geophysics Incorporated
NRL	Naval Research Laboratory
RMS	Root Mean Square
RTK	Real Time Kinematic
RTS	Robotic Total Station
SERDP	Strategic Environmental Research & Development Program
SNR	Signal to Noise Ratio
TtFW	Tetratech Foster-Wheeler
UXO	Unexploded Ordnance
YPG	Yuma Proving Ground

1. Introduction

1.1 Background

The Standardized UXO Technology Demonstration Sites were established by the Environmental Security Technology Certification Program (ESTCP) under project MM-0103 to ensure that critical unexploded ordnance (UXO) technology performance parameters such as detection capability, false alarm rates, discrimination, reacquisition, and system efficiency are determined through standardized test methodologies, procedures, and facilities. This project has performed standardized analyses of data collected at the two standardized sites at Aberdeen Proving Ground (APG) in Maryland and Yuma Proving Ground (YPG) in Arizona in order to understand the factors that affect UXO detection and discrimination. We focus on electromagnetic induction (EMI) sensor and total field magnetometer systems. The EMI sensors (EM61 and EM63) excite eddy currents in the target with an electromagnetic pulse (primary field) and measure the induced field associated with the eddy current decay at a range of times after the primary field cutoff. The magnetometers measure distortions of the earth's magnetic field caused by ferromagnetic targets.

The standardized sites and the data sets used in the analyses reported here are described in §2. The demonstrator data sets analyzed in this project were collected by the Naval Research Laboratory (NRL), Tetra Tech Foster Wheeler, Inc. (TtFW), Army Corps of Engineers Engineering Research and Development Center in Vicksburg (ERDC), Shaw Environmental, Inc., and NAEVA Geophysics. The analysis focused primarily on systems using total field magnetometers and systems based on the EM61 MkII time-domain EMI sensor. ERDC used the EM63 sensor. It is similar to the EM61, but measures the EMI response over a greater range of time decay than the EM61. Section 2 also includes brief discussions of the physical principles of the sensors and the interpretation of data collected using the sensors.

1.2 Technical Approach

The analysis approach used in this project is based the standard dipole response model wherein the magnetic or electromagnetic response of a target is represented by an induced dipole moment at the target location. Spatially mapped data collected over the target are inverted using this model to determine the target's location and depth and the parameters or features which characterize the target response. For the EMI sensors these are the three principal axis polarizabilities, which convey information about the size and shape of the target [1]. For magnetic sensors, the features are the strength and orientation of the target's magnetic dipole moment, which convey information about the target size and any significant remnant magnetization [2, 3]. The analyses were intended to be statistical in nature, based on large numbers of targets and designed to reveal general capability dependencies. However, in as much as they rely on the availability of target ground truth data, the results have ended up being somewhat limited.

Performance metrics used in the analyses include target signal-to-noise-ratio (SNR), dipole fit quality (squared correlation between the data and the dipole model fit to the data) and the accuracy of target depth and target parameter estimates (size, polarizabilities) which are used for target classification and discrimination.

The target SNR used here is the ratio of the peak signal strength squared to noise variance. Signal strength is calculated using a dipole model fit to the anomaly, interpolated over a finely-spaced grid to ensure capture of the model peak signal strength. We do this because on any survey the tracks will not necessarily intersect the anomaly peak anomaly. The noise level is estimated individually for each target

from a neighboring survey area that contains no obvious anomalies. With carefully collected data, dipole fit quality increases with target SNR in a predictable way, so comparisons of dipole fit quality and SNR help to establish if poor fits are due to weak signals and/or high noise levels or to data collection problems. Target characterization and discrimination is based on the target parameters or features determined from inversion of the data using the dipole response model. Dipole fit quality is generally the best indicator of the fidelity of the calculated target parameters.

The EMI data analysis is reported in §3. This section begins with a discussion of the procedures for processing EMI data and extracting target parameters or features and how those parameters are related to target size and shape. Target depth estimation results are presented in §3.1. Depth estimates generally improve with fit quality. Most of the estimated depths are within ±25 cm, but even with the targets restricted to fit quality greater than 0.98 there are significant outliers. Size estimation results are presented in §3.2. Again, there are some significant outliers (which generally correspond to targets for which the depth was overestimated), but for the bulk of the data the target size estimates vary with UXO caliber as predicted by theory.

The target shape parameters and implications for UXO/clutter discrimination are discussed in §§3.3 and 3.4, respectively. Some classification and discrimination on the basis of target size may be possible at limited-use sites where the UXO have a narrow size range. However, given the overall data quality in the surveys analyzed here, shape-based discrimination is problematic. We believe that be basic problem is geolocation errors which effectively add a substantial noise component to the dipole inversion, significantly degrading the accuracy of the estimated target features.

Results from the magnetometer analysis are reported in §4. The relationship between dipole fit quality and SNR is discussed in §4.1, and results on target size and depth estimates in §4.2. Very accurate depth estimates are obtained with data having fit quality greater than 0.98. For these data, the size estimates are consistent with historical data. Evidence of remnant magnetization effects is briefly discussed in §4.3. The analysis is based on a comparison of results from degaussed and non-degaussed UXO targets, and no significant differences between target parameter distributions for the two classes were observed.

Overlapping target signatures are considered briefly in §5, which looks at what happens when standard dipole fitting procedures are used on data that contain response contributions from two targets. We see no significant differences between fit quality distributions for single and multiple targets. Presumably this is because the fit quality is not particularly good in general, and perhaps because the fits for some of the double targets are dominated by one or the other of the targets.

Generally speaking the results are disappointing. Only a relatively small fraction of the survey data analyzed here is accurate enough to support reliable feature-based target classification and discrimination. Even when the target SNR is relatively high the dipole fit quality is frequently relatively poor, suggesting that the problems are due to deficiencies in the surveys, especially sensor location errors.

2. Standardized Sites

2.1 Site Descriptions

The data were all collected at the Standardized UXO Technology Demonstration Sites at Aberdeen Proving Ground (APG) and Yuma Proving Ground (YPG). These standardized test sites have been used to benchmark a significant number of technologies and contractors. The two sites represent different geological/geophysical environments that affect magnetometers and EMI sensors in different ways but each standardized site consists of three main areas: a calibration lane, a blind grid, and an open field. The calibration lane allows demonstrators to test their equipment with a standardized target repository, build a site library, document signal strength, and address site-specific variables. The blind grid allows demonstrators to showcase the sensors on their system without platform, coordinate system, or operational concerns. The open field documents the performance of the entire system in actual range operations.

The APG Standardized Test Site is located about 30 miles northeast of Baltimore, within a secured range area of the Aberdeen Proving Ground, adjacent to the Trench Warfare facility. It encompasses 17 acres of upland and lowland flats, woods and wetlands. Figure 1 (left) shows an aerial map of the APG site. The site contains several field scenarios, and the open field area at Aberdeen contains a number of challenge areas. The various areas are either numbered or labeled in the figure. The site is divided into areas, including calibration lanes, a blind test grid, and three particular scenarios: open field, moguls (7), and trees (8). The challenges in the open field scenario are: electrical lines (1), wet areas (2), swales (3), stone pad/road area (4), high density clutter (5) and steel fencing (6).

The YPG Standardized Test Site is located 26 miles north of Yuma Arizona, within an area of the Yuma Proving Ground. It is adjacent to the Colorado River in the Sonoran Desert of Southwest Arizona, one of the hottest and driest areas in the nation, where the average rainfall is about three inches. The climate and terrain are similar to major desert areas worldwide. Figure 1 (right) shows an aerial map of the YPG Standardized Test Site. Like APG, the site (about 20 acres) contains several different field scenarios. There is an open field range, calibration grid, blind test grid, mogul area, and desert extreme area. The open field site is the largest of the test sites and measures approximately 200 m by 350 m. The calibration and blind test grids measure 30 m by 40 m and 40 m by 40 m, respectively. South of the open field is the 135 m by 80 m mogul area consisting of a sequence of man-made depressions. The desert extreme area is located south east of the open field site and has dimensions of 50 m by 100 m. The desert extreme area, covered with desert-type vegetation, is used to test the performance of different sensor platforms in a more severe desert environment.

2.2 Data Sets

Data from APG and YPG collected by various performers over the Blind Grid and the Open Field were analyzed. From our previous experience with these performers and the data, as well as from the published performance reports, we selected data that covered a range of performance capabilities. However, after the first look at some of the performer data, we eliminated some that were clearly inadequate for yielding insight into general survey capabilities, due to poor data leveling, large position errors or sensor drift.

The demonstrator data sets analyzed in this project were collected by the Naval Research Laboratory (NRL), Tetra Tech Foster Wheeler, Inc. (TtFW), Army Corps of Engineers Engineering Research and Development Center in Vicksburg (ERDC), Shaw Environmental, Inc., and NAEVA Geophysics. The

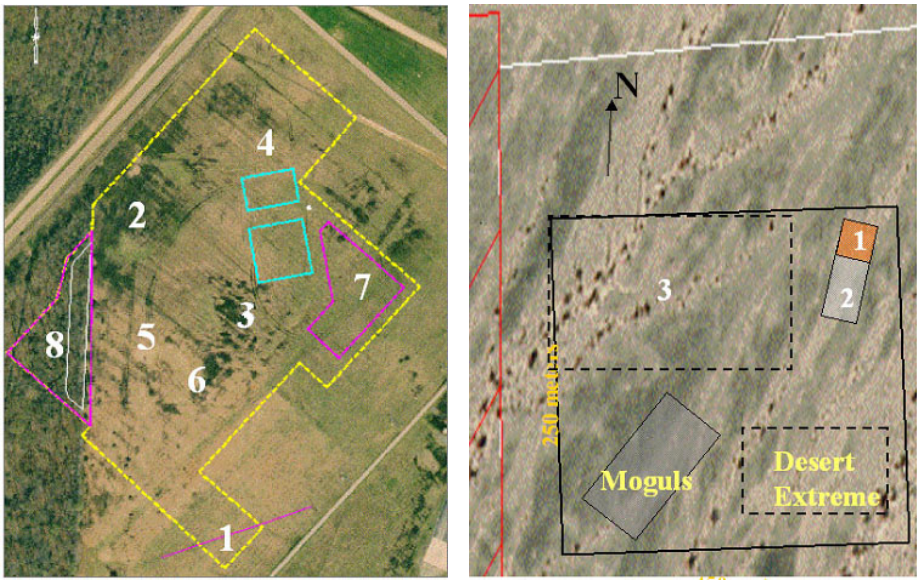

Figure 1. Standardized UXO demonstration sites at Aberdeen Proving Ground (left) and Yuma Proving Ground (right).

analysis focused primarily on systems using total field magnetometers and systems based on the EM61 MkII time-domain EMI sensor. ERDC used the EM63 sensor. It is similar to the EM61, but measures the EMI response over a greater range of time decay than the EM61. Table 1 shows the demonstrators and data sets analyzed to obtain the results presented here, along with the number of UXO and clutter items analyzed for each area. All targets analyzed had ground truth available, were not multiple targets (see §5 below) and were isolated from nearby anomalies (at least 2 meters away).

Table 1. Data Sets Analyzed

Demonstrator	**APG Blind Grid**	**APG Open Field**	**YPG BlindGrid**	**YPG OpenField**	**Comments**
	# UXO and clutter analyzed	*# UXO and clutter analyzed*	*# UXO and clutter analyzed*	*# UXO and clutter analyzed*	
magnetometer					
Shaw	30/31			*(poor data)*	
NRL MTADS	29/32	47/42	21/0	58/0	0.25 m lanes
EMI data					
TtFW EM61MkII				186/86	0.5 m lanes
NRL MTADS EM61MkII	*(no data collected)**	86/98			
ERDC EM63	65/0				
NAEVA EM61			69/93	150/70	¾-1 m lanes

***** the Blind Grid was reconfigured before data could be collected

The EM61 MkII is a time-domain electromagnetic instrument designed to detect shallow ferrous and nonferrous metallic objects. The applicability of the EM61 for UXO detection has been widely demonstrated at sites across the United States. It operates by transmitting a magnetic pulse that induces eddy currents in any nearby conducting objects. These currents induce secondary magnetic fields that are measured by the sensor after the transmitter pulse has ended. The sensor response is the voltage induced in the receiver coil by these secondary fields, and is proportional to the time rate of change of the magnetic flux through the coil. The sensor integrates this induced voltage over a fixed time gate and averages over a number of pulses. The NRL MTADS EM61 array (Figure 2, inset picture) consists of three overlapping 1m by 1m coils. An illustration of the magnitude and direction of the field transmitted by the MTADS array is shown in the diagram in Figure 2. Note that the field experienced by an object directly below the array is substantially different than an object in front of or behind the array. This allows the system to get several "looks" at the target as the array passes over it, which is important for estimating target parameters from the data.

Processing of the EM61 relies on the fact that the signal is a linear function of the flux through the receiving coil. The flux is assumed to originate from an induced dipole at the target location with dipole moment given by

$$\mathbf{m} = \mathbf{UBU}^{\mathbf{T}} \cdot \mathbf{H}_0 . \tag{1}$$

Here **H**o is the peak primary field at the target, **U** is the transformation matrix between the coordinate directions and the principal axes of the target, and **B** is an empirically-determined, effective magnetic polarizability matrix. For any arbitrary compact object, this matrix can be diagonalized about three primary body axes and written as

$$\mathbf{B} = \begin{pmatrix} \beta_X & 0 & 0 \\ 0 & \beta_Y & 0 \\ 0 & 0 & \beta_Z \end{pmatrix} . \tag{2}$$

For an axially symmetric object, **B** has only two unique coefficients, corresponding to the longitudinal (β_L) and transverse (β_T) directions:

$$\mathbf{B} = \begin{pmatrix} \beta_L & 0 & 0 \\ 0 & \beta_T & 0 \\ 0 & 0 & \beta_T \end{pmatrix} . \tag{3}$$

Empirically, we observe that for elongated ferrous objects such as cylinders and most UXO, the longitudinal coefficient is greater than the transverse coefficient. For flat ferrous objects such as disks and plates, the opposite is true. This matches the behavior of these objects in the magnetostatic limit. For non-ferrous objects such as aluminum cylinders and plates, these relationships are reversed.

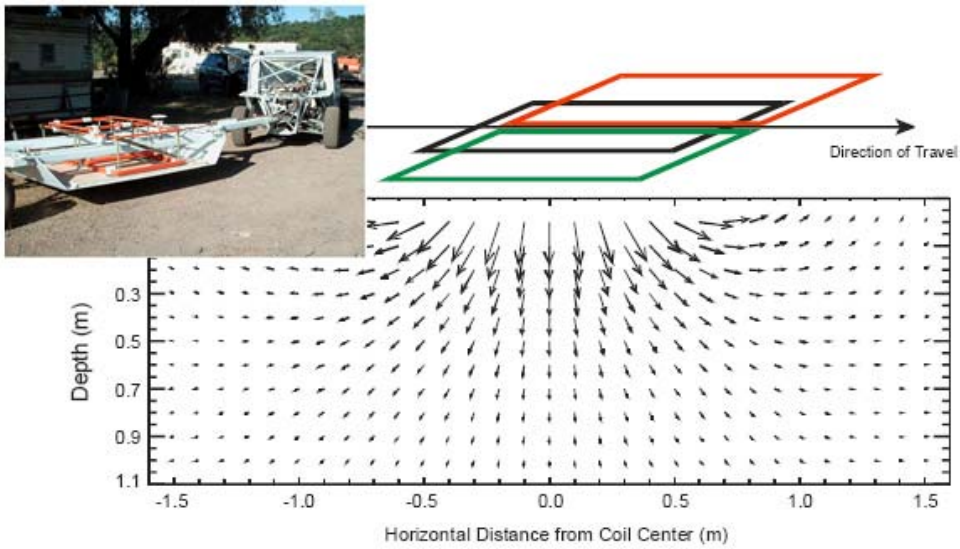

Figure 2. NRL MTADS EM61 array (inset) and diagram of EMI field below the array.

The other EMI demonstration systems are shown in Figure 3. Both NAEVA Geophysics EM61 MkII systems that were used at YPG had 1m by 0.5m coils. The man-portable system (Figure 3a) was used for the Blind Grid, and the towed array (Figure 3b) was used for the Open Field. The NAEVA towed array system has two sets of coils encased in a polyplastic sled that rests directly on the ground. Coil heights can be adjusted using inflatable air bladders within the sled and were maintained at the standard height of 40 cm above the ground for the demonstration. The system is towed by an eight-wheeled Argo all-terrain vehicle. A 16-foot tongue attaches the coil assembly to the Argo and maintains sufficient separation so that the vehicle does not influence the geophysical data. Both systems use real-time differential GPS (DGPS) data positioning. In the case of the towed array, the rover antenna is mounted between the two coils and an offset is applied during the post-processing to produce the actual coil positions. The rover antenna is mounted directly over the single coil in the man-portable system. The EM61 MkII system used by TtFW is shown in Figure 3c. It had 1m by 1m coils and used Arc Second Constellation, and Leica Series 1100 Robotic Total Station laser positioning systems. The ERDC EM63 system is shown in Figure 3d. The EM63 is similar to the EM61, but measures the EMI response over a greater range of time decay. Local positioning and georeferencing of the ERDC EM63 system was accomplished using a Trimble 5700 real time kinematic (RTK) GPS system. Further details of the various systems can be found in documents that can be downloaded from the Standardized UXO Technology Demonstration Sites Program web site at http://aec.army.mil/usaec/ technology/uxo03.html.

Anomaly maps of the NAEVA EM61 surveys at YPG are shown in Figure 4. The survey is shown as a false color map. Background levels are green, with increasing signal strength tending up through yellow to red. The red patches or spots show EMI field anomalies caused by buried metal objects, both UXO and clutter. Anomaly maps for APG are shown in Figure 5. The Blind Grid map on the left is from the ERDC EM63 survey, using time gate 10, which corresponds to the third gate for the standard EM61 MkII. The Open Field map on the right is from the MTADS EM61 survey. The sensors in the NRL system are specially modified by Geonics to make them more compatible with vehicular speeds and to increase their sensitivity to small objects. They have four sample gates, two sampling both the top and bottom receive coils early in the decay and the other two sampling the bottom coil at progressively later times.

Figure 3. EMI demonstration systems: (a) NAEVA Geophysics manportable EM61, (b) NAEVA Geophysics EM61 towed array, (c) TtFW EM61, (d) ERDC EM63.

The total field magnetometer systems measure distortions of the earth's magnetic field caused by ferromagnetic objects. This distortion or magnetic field anomaly can also be expressed in terms of a dipole field. For a highly permeable sphere, the induced dipole moment is given simply by

(4) $$\mathbf{m} = 4\pi a^3 \mathbf{H}_0$$

where a is the radius of the sphere and $\mathbf{H}_0$ is the geomagnetic field. For UXO and UXO-like objects we can represent the dipole moment in terms of a demagnetization tensor, and measured variations in the strength of the induced dipole moment with target orientation relative to the earth's field can be accurately modeled using appropriate demagnetization factors [1].

Magnetometer survey maps for APG and YPG are shown in Figure 6. The Shaw magnetometer pushcart and the MTADS towed magnetometer array that were used in the surveys are shown in Figure 7. The Shaw UXO Mapper has several components: G858 total field magnetometer sensors, Shaw's composite-material cart survey system, and a Leica TPS1100 dual laser robotic total station (RTS) combined with a Crossbow solid-state gyro for sensor positioning. The MTADS system consists of an array of 8 total field magnetometers towed behind a low magnetic signature vehicle. Sensor positioning is handled using a differential GPS system.

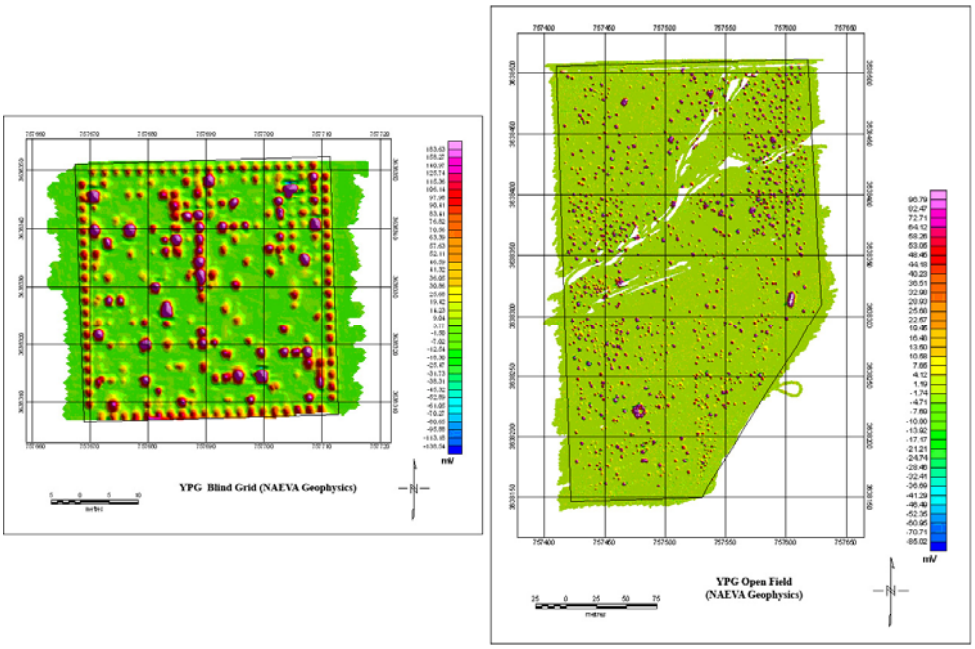

Figure 4. NAEVA EM61 survey maps for YPG Blind Grid (left) and Open Field (right).

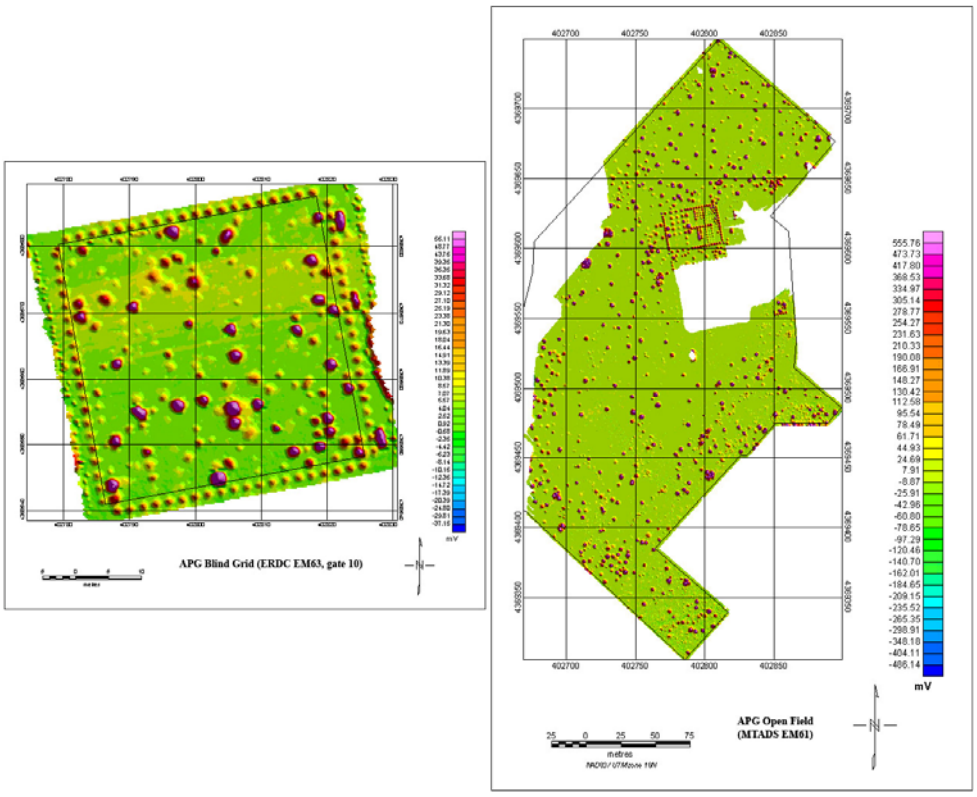

Figure 5. APG survey maps. ERDC EM63 survey of Blind Grid on the left, and NRL survey of the Open Field on the right.

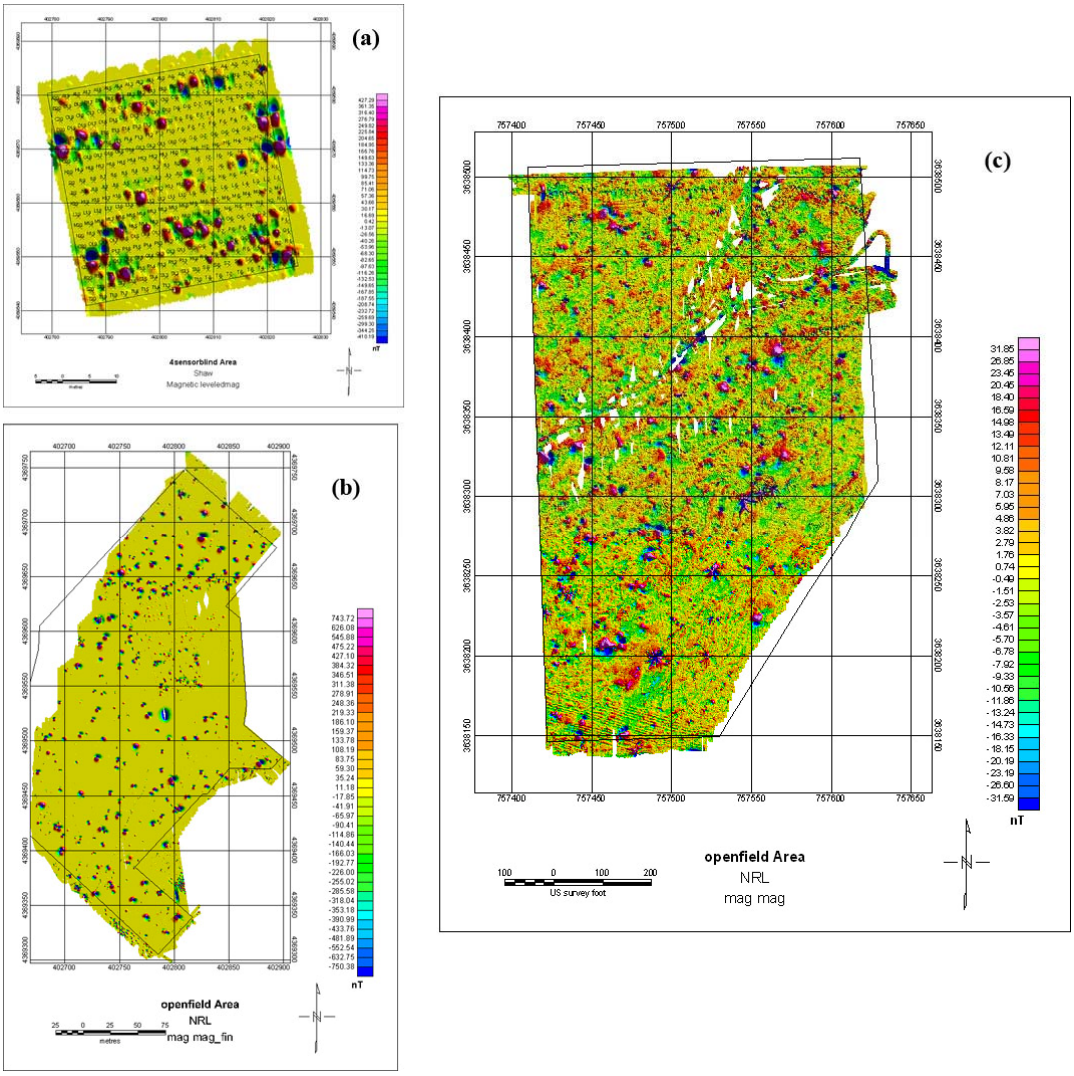

Figure 6. Magnetometer surveys. (a) Shaw survey of APG Blind Grid, (b) MTADS survey of APG Open Field, (c) MTADS survey of YPG Open Field.

Figure 7. Shaw pushcart magnetometer system (left) and MTADS towed magnetometer array (right).

3. EMI Data Analysis

The raw signature data from an EMI sensor reflects details of the sensor/target geometry as well as inherent EMI response characteristics of the targets themselves. In order to separate out the intrinsic target response properties from sensor/target geometry effects we invert the signature data to estimate principal axis magnetic polarizabilities for the targets. The EMI data are inverted using the standard induced dipole response model wherein the effect of eddy currents set up in the target by the primary field is represented by a set of three orthogonal magnetic dipoles at the target location [4]. As noted previously, the measured signal is a linear function of the induced dipole moment **m**, which can be expressed in terms of a time dependent polarizability tensor **B** in accordance with equation (1). Given a set of measurements of the target response with varying geometries or "look angles" at the target, the data can be inverted to determine the (X, Y, Z) location of the target, the orientation of its principal axes (ψ, θ, ϕ), and the principal axis polarizabilities (β_1, β_2, β_3) which are the eigenvalues of **B**. The basic idea is to search out the set of nine parameters (X, Y, Z, ψ, θ, ϕ, β_1, β_2, β_3) that minimizes the difference between the measured responses and those calculated using the dipole response model.

The EMI sensors (EM61 and EM63) measure the induced field decay at a range of times after the primary field cutoff. The inversion of these data can proceed assuming that the principal axis directions (ψ, θ, ϕ) are either fixed in time or vary during the course of the decay. We examined this issue using the EM63 data and found that the measured response was consistent with fixed principal axis directions. Figure 8 shows a comparison of inversion results for APG Blind Grid target T12 (a clutter item) with the principal axis angles fixed (dashed) and allowed to vary with decay time (solid). Different colors correspond to the three different principal axis polarizabilities. There are no significant differences between the two sets of polarizabilities.

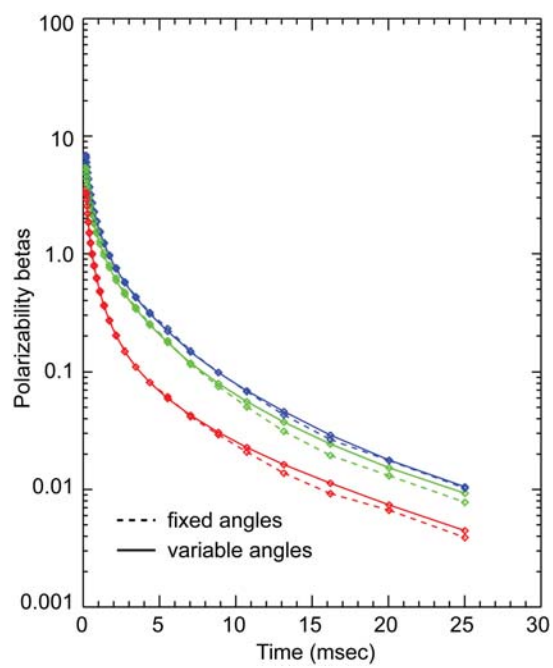

Figure 8. Comparison of EM63 inversion with principal axis angles fixed in time or variable.

The principal axis polarizabilities contain information about the size and shape of the target: target size determines the overall magnitude of the βs, while target shape determines the differences among the three βs for the target. For EM61 signatures of UXO items, we have one large β corresponding to an axially excited dipole and two smaller, equal βs corresponding to transverse excitation, perpendicular to the long axis of the UXO item. Figure 9 shows the results of an analysis of first time gate data collected with a handheld EM61 sensor on a test stand over various UXO and clutter items in ESTCP project MM-0108. In this plot the primary beta value (β_1) is plotted along the horizontal axis. The average of the two secondary betas (β_2 and β_3) is plotted along the vertical axis, and the vertical line stretches between the values of the secondary betas. The beta values for the ordnance are as expected: the larger ordnance items have larger βs, clustered close to a different point for each ordnance type, and the two secondary betas are smaller and equal. The beta values for the clutter are scattered, with secondary beta values usually different from each other.

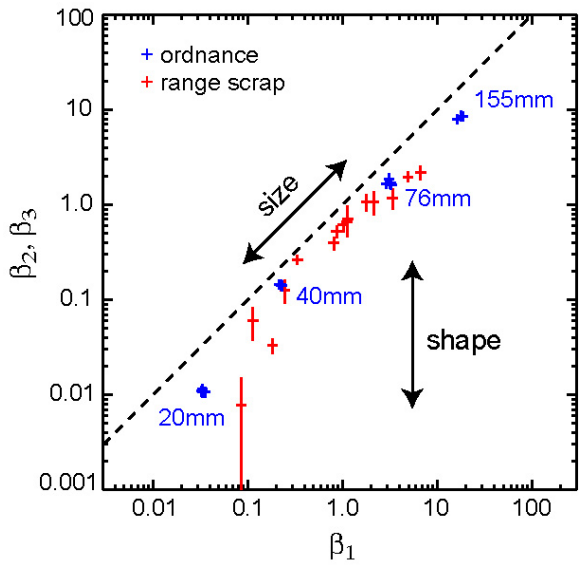

Figure 9. Beta values for various UXO and clutter items.

Current discrimination techniques rely on inverting spatially mapped EMI data to estimate the polarizability tensor and its eigenvalues. However, since EMI signatures are typically not very sensitive to variations in target features, relatively small amounts of noise (including errors in spatial mapping of the data) can produce errors in target parameters large enough to make reliable target discrimination impossible. In what follows, we will use the dipole fit quality as a measure of how well the data can be represented using the standard dipole response model. Dipole fit quality (ρ^2) is defined as the squared correlation coefficient between the data and the dipole model fit. The RMS mismatch between the data and the model fit (dipole fit error) is equal to $\sqrt{(1 - \rho^2)}$. Dipole fit qualities of 0.99 and higher are possible with carefully collected, high signal to noise ratio (SNR) data [5]. Poor fit quality is generally an indicator that the fidelity of the measured EMI response of the target is not good enough to support accurate dipole inversion and estimation of target parameters. As a practical matter, dipole fit quality generally improves with increasing target SNR. Figure 10 shows dipole fit quality *vs.* SNR for the TtFW data. SNR is based on peak anomaly signal strength and an estimate of RMS noise from a nearby, target-free data patch. Fit quality degrades rapidly below about 40dB.

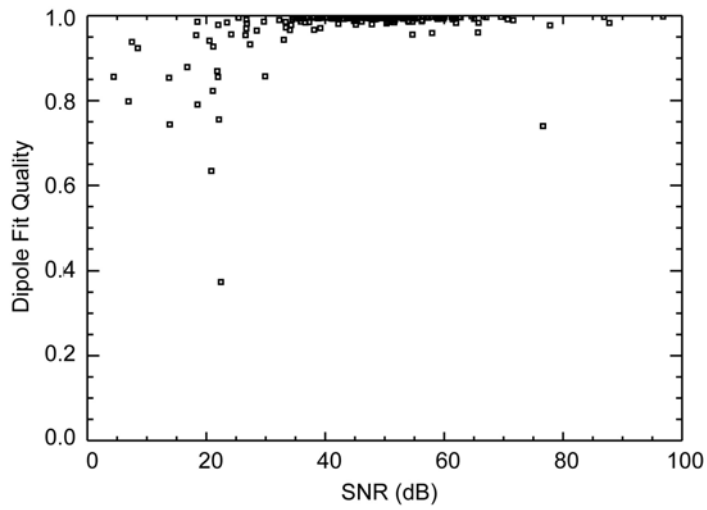

Figure 10. Dipole fit quality *vs.* SNR for the TtFW EM61 data.

3.1 Target Depth Estimation Results

The dipole inversion produces an estimate of the location of the target. This is actually the location of a three-axis point dipole that best reproduces the measured signal, and as such corresponds loosely to the location of the center of the target. Figure 11 shows comparisons between target depth estimates and ground truth depths for the TtFW EM61 survey data. The three plots are intended to show the effect of dipole fit quality on the accuracy of the depth estimates. The plot on the left includes all of the targets, while the one in the middle and the one on the right are restricted to those targets for which $\rho^2 > 0.98$ and 0.997, respectively. On average, the depth estimates seem to improve with fit quality.

Estimated depths from the different EMI surveys are compared with ground truth depths in Figure 12. Only targets for which the dipole fit quality is greater than 0.98 (~15% RMS mismatch between the data and the dipole fit) are included. The TtFW EM61 results are shown in gray, the NAEVA EM61 in blue, the MTADS EM61 array results in green and the ERDC EM63 results in red. They are all similar, with

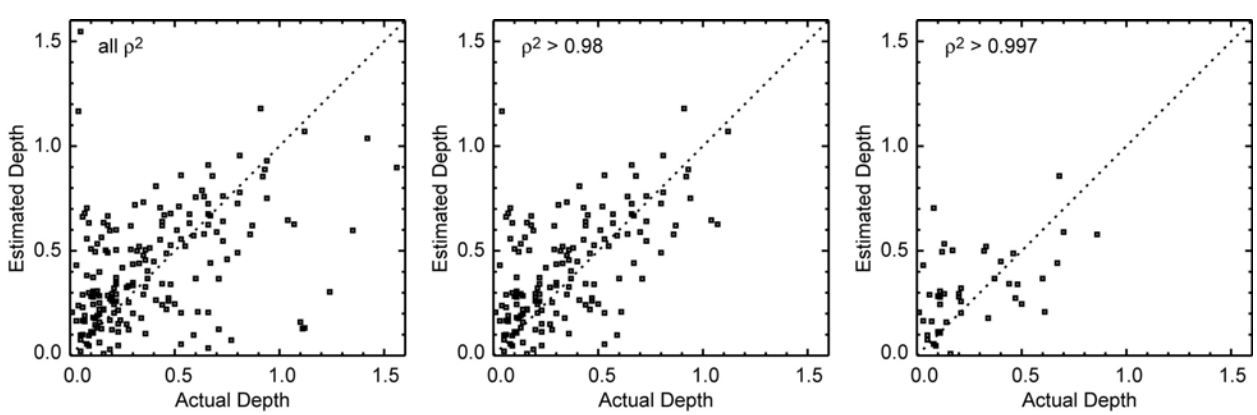

Figure 11. Target depth estimates (in meters) from TtFW EM61 survey data compared with ground truth depths.

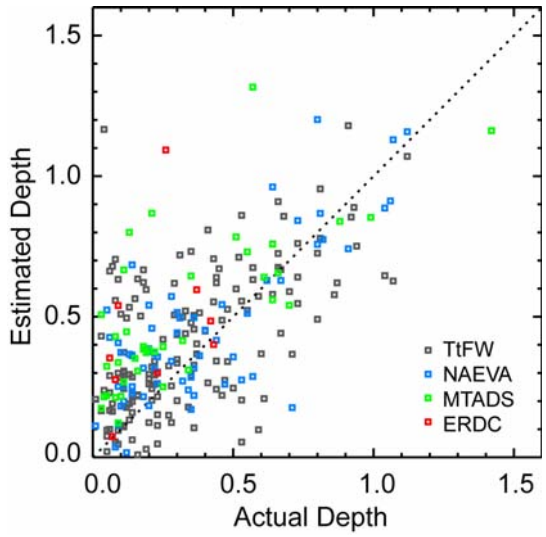

Figure 12. Estimated depths from the different EMI surveys compared with ground truth depths.

the data scattered more or less evenly about the diagonal. These results show the sort of depth estimation accuracy that can be expected with carefully collected EMI survey data. Even with the targets restricted to fit quality greater than 0.98 there are significant outliers, although most of the estimated depths are within 25 cm of the true target depth.

3.2 Target Size Estimation Results

The net polarizability should scale with target size, although the scaling is complicated by the fact that we measure the EMI signal at a fixed time after primary field cutoff. The overall EMI response is proportional to the volume of a compact steel target [6]. It initially decays with time after the primary field cutoff as $t^{-1/2}$, transitions to $t^{-3/2}$ at a time that is proportional to the linear size of the target, and eventually decays exponentially at late times [7]. The time at which the response transitions from $t^{-1/2}$ to $t^{-3/2}$ is referred to as the magnetic crossover time t_M, and it is proportional to the characteristic length scale L of the target. Varying L slides the response curve back and forth in time. Consequently, at a fixed time t_0 in this regime, the response should scale as something like $L^{3.5}$ or $L^{4.5}$ depending on the value of t_M, relative to t_0. The response will scale more rapidly with size in the exponential regime, but for most UXO and UXO-like targets this occurs at times later than the EM61 measures (*i.e.*, >1.3 msec). Also, for all but the smallest items the $t^{-1/2}$ regime occurs at times earlier than the EM61 measures (*i.e.*, <0.22 msec) [8].

The trace of the polarizability tensor is a convenient measure of the net strength of the response. It is invariant to target orientation and hence equal to the sum of the eigenvalues ($\Sigma\beta_i$). Roughly speaking, we expect that the representative target length scale can be estimated using the relationship

(5) $$L \propto \left(\sum \beta_i\right)^{1/4}$$

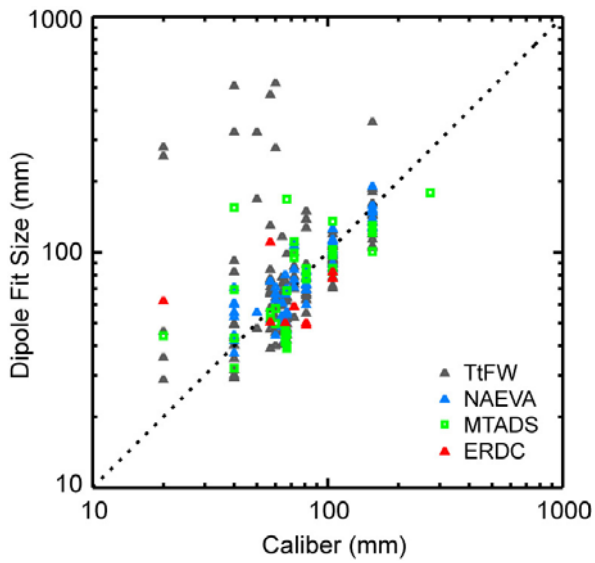

Figure 13. Apparent target size from dipole fit *vs.* caliber for UXO targets.

with proportionality constant determined by the sensor characteristics. Figure 13 shows the results of EMI-based target size estimates for the various demonstrators. Proportionality constants were chosen so that on average the length scale estimates matched up with UXO caliber. First time gate data were used for the EM61 surveys (TtFW, NAEVA and MTADS). The 5th time gate was used for the EM63 (ERDC) data. As with Figure 12, only targets for which $\rho^2 > 0.98$ were used in the plot. There are about a dozen outliers which generally correspond to targets for which the depth was significantly overestimated. For the rest of the data the target size estimates vary with caliber as predicted by equation (5). The spread is consistent with our general experience for target size estimates [2]. As with the target depth estimates, there is little difference among the demonstrators.

3.3 Target Shape Parameters

The interrelationships among the principal axis polarizabilities are determined by the shape of the target. Most UXO are designed to be shot from guns and travel along stable trajectories to their target. Consequently UXO are typically cylindrically shaped. The along-axis polarizability is generally greater than the two (degenerate, equal) cross-axis polarizabilities. Figure 14 and Figure 15 are β-plots for UXO targets from the TtFW and MTADS EM61 surveys. As in Figure 9 the largest or primary polarizability (β_1) is plotted along the horizontal axis, and the secondary polarizabilities are plotted along the vertical axis. The symbol is plotted at the average of β_2 and β_3, while the vertical line runs from β_2 to β_3. Each set of plots shows the progression as we screen the results by fit quality, from all UXO targets on the left, to those with $\rho^2 > 0.90$ in the center, and those with $\rho^2 > 0.99$ on the right. All of the targets should line up slightly below the diagonal, and the spread between β_2 and β_3 (as reflected by the length of the vertical line) should be small compared to the average of β_2 and β_3. This is clearly not the case for the majority of the targets in either survey, and indeed is not even the case for all of the (relatively few) targets with fit quality greater than 0.99. Figure 16 shows the corresponding results for ERDC and NEAVA UXO targets with $\rho^2 > 0.99$.

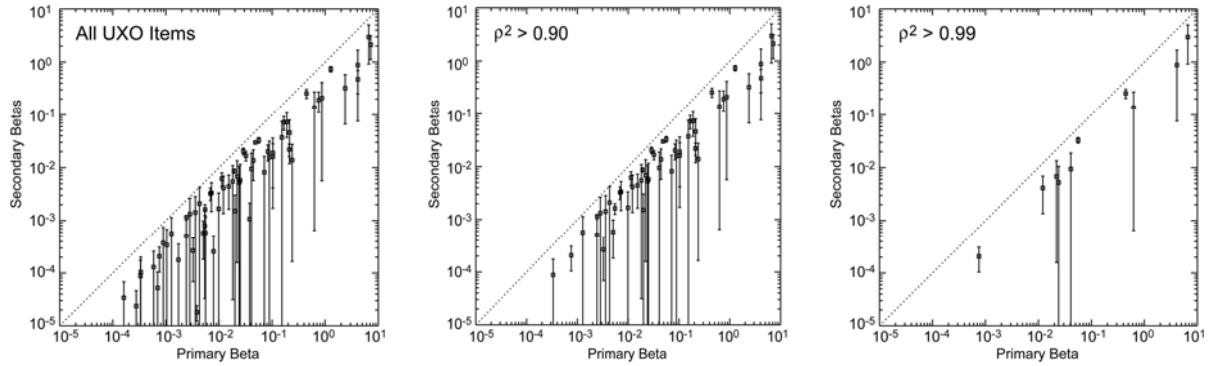

Figure 14. UXO polarizabilities from TtFW EM61 survey data.

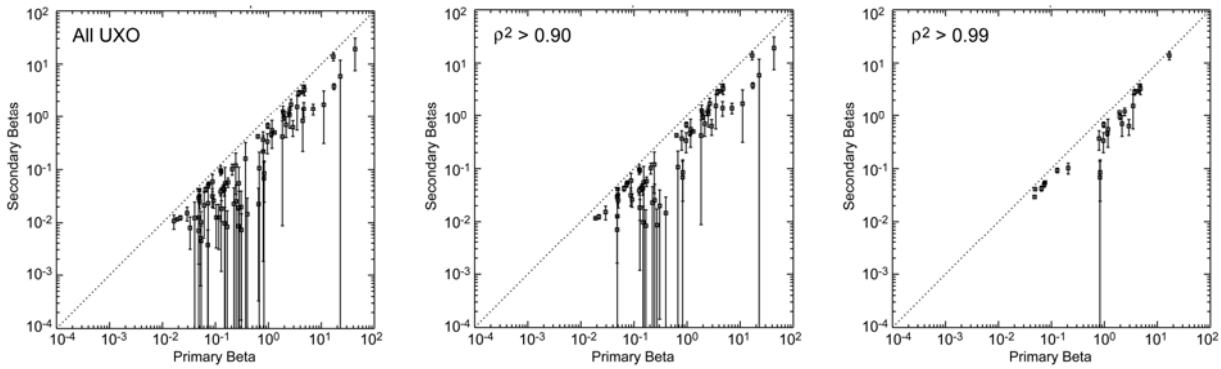

Figure 15. UXO polarizabilities from MTADS EM61array survey data.

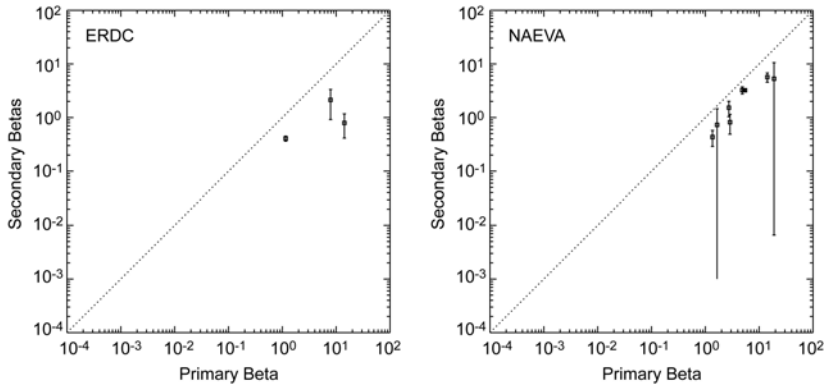

Figure 16. UXO polarizabilities from ERDC and NAEVA survey data, fit quality > 0.99.

3.4 UXO/Clutter Discrimination

At issue is whether or not the features (principal axis polarizabilities) estimated from the EMI survey data can support target classification and discrimination. Qualitatively, in the preceding figures the MTADS βs for fit quality > 0.99 look the best. Figure 17 shows a comparison of MTADS βs for UXO and clutter items (with $\rho^2 > 0.99$). One's first impression might be that there is little to distinguish the two distributions. This is certainly appears to be true insofar as the target shape measures (ratio of primary to secondary βs and relative spread of the secondary βs) are concerned. However, we do see some evidence of grouping or clustering in the UXO βs similar to that seen in Figure 9. Fourteen different ordnance types ranging in size from submunitions to 155 mm projectiles were emplaced at the standardized sites. If we were dealing with only one or two ordnance types, the spread in the UXO βs along the diagonal would be significantly reduced relative to that of the clutter, providing a measure of discrimination capability based on target size.

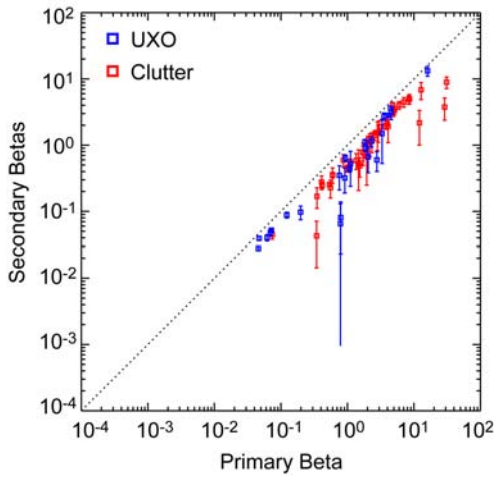

Figure 17. UXO and clutter betas from MTADS EM61 array survey data, fit quality > 0.99.

Quantitatively, how well a buried UXO item can be distinguished from clutter depends on the errors or uncertainty in the UXO item's estimated βs. If the estimates spread out in a diffuse cloud, the discrimination capability is less than when they are tightly grouped. Target SNR and positioning errors are the primary factors affecting the spread in the observed "beta cloud" for a particular UXO target [9, 10]. This is illustrated in Figure 18, which shows the effects of noise and positioning errors on dipole model fit errors. Dipole fit error is the RMS difference between the EM61 data and the dipole model fit to the data. The data were from EM61 surveys done under SERDP project MM-1310 (Sensor Orientation Effects on UXO Geophysical Target Discrimination). The symbols show dipole model fit error vs. target SNR from the inversion of the spatially mapped EM61 data. The solid line shows the expected dependence of fit error on SNR assuming that the sensor positions corresponding to the EM61 signal measurements were correctly known. The dashed line shows the expected behavior assuming 9 cm uncertainty in the actual locations of the measurements. This seems to match the observed trend in the data, leaving a residual fit error of about 15%. Analysis results presented at the June 2005 SERDP/ESTCP Geolocation Workshop show that 15% dipole fit errors can result in complete (100%) uncertainty in estimates of the polarizability tensor [11]. Thus, both high SNR (greater than 30 dB) and small geolocation errors are required in order to accurately estimate target features useful for UXO/clutter discrimination (i.e., the principal axis polarizabilities or βs).

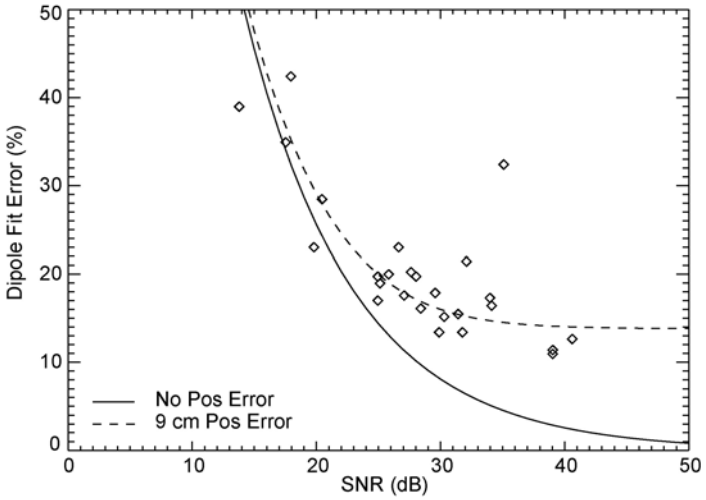

Figure 18. Dipole model fit error *vs.* target signal to noise ratio (SNR) for EM61 data collected in SERDP project MM-1310.

4. Magnetometer Data Analysis

Magnetometers sense distortions in the earth's magnetic field caused by buried UXO and other ferrous objects. The magnetic anomaly pattern has a simple characteristic form determined by the strength and orientation of the target's magnetic dipole moment, and the magnetometer survey data can be inverted using a dipole response model, yielding estimates of the target's location, size and depth [2, 12]. The inversion uses a modified gradient search technique to determine the location, strength and orientation of the magnetic dipole whose field anomaly best matches the measured data. An apparent target size (a) is inferred from the dipole moment using equation (4). It is the radius of a steel sphere which has the same magnetic dipole moment as the target. This apparent target size does not correspond exactly to the physical dimensions of the target for several reasons. In addition to the locally induced field, the object may contain permanent or remnant magnetization. Depending on the strength and orientation of the permanent moment relative to the induced moment, the size inferred from the net moment using equation (4) may be larger or smaller than the actual size of the object. Also, if the object is elongated, the strength of the induced field, and hence the apparent size, will depend on the orientation of its axis relative to the earth's field. On average, we have observed that for UXO the apparent size is roughly equal to the caliber of the object, with a variability of about ±25% RMS [2, 12]. Targets with significant remnant magnetic moments can have dipole orientations that are significantly misaligned with the earth's field, which in some cases can be useful for UXO/clutter discrimination [3].

4.1 Dipole Fit Quality and SNR

As with the EMI data, there is a general trend of increasing dipole fit quality (ρ^2) with SNR for magnetometer data. Figure 19 shows results for the MTADS magnetometer array and the Shaw pushcart. As with the EMI data in Figure 10, SNR is based on the peak anomaly signal strength and an estimate of RMS noise from a nearby, target-free data patch. Generally, the MTADS data show higher dipole fit quality than the Shaw data. The basic problem is illustrated in Figure 20. This plot shows 6m by 6m patches of MTADS and Shaw magnetometer data for one of the targets (location E07) in the APG Blind Grid. Each dot represents one magnetometer reading, with color scale running from -20 nT (dark blue) to +20 nT (bright red). The anomaly is clearly better resolved and represented in the MTADS data. This is reflected in the respective fit qualities, $\rho^2 = 0.967$ for the MTADS data, and $\rho^2 = 0.775$ for the Shaw data.

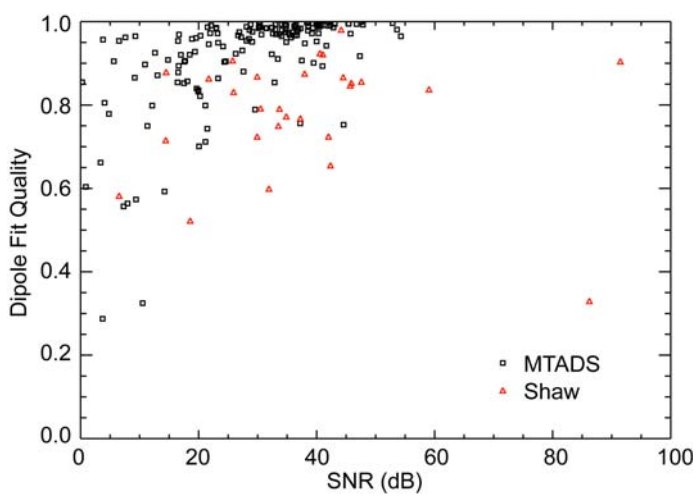

Figure 19. Magnetic dipole fit quality *vs.* SNR for Shaw pushcart and MTADS magnetometer array.

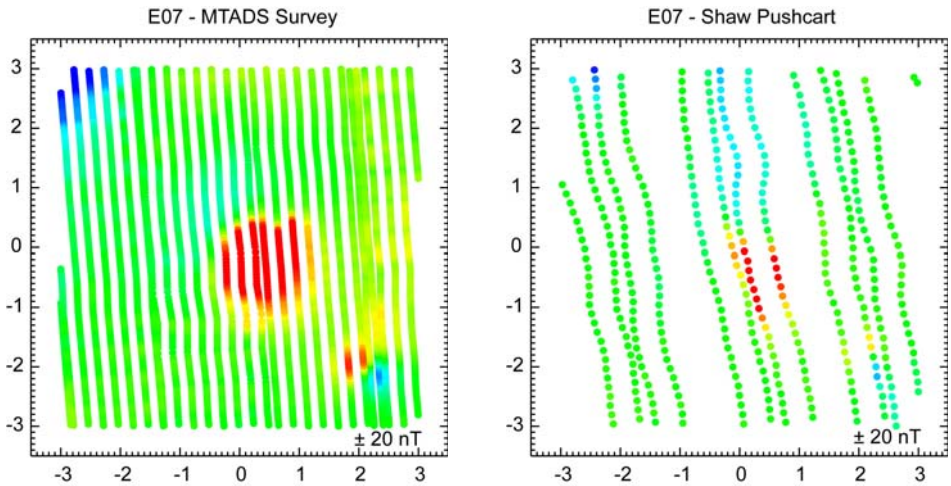

Figure 20. Comparison of MTADS and Shaw data for anomaly E07 in APG Blind Grid.

4.2 Target Size and Depth

Figure 21 shows comparisons between target depth estimates and ground truth depths for the MTADS magnetometer array data. The plot on the left includes all of the targets regardless of fit quality. The middle plot is restricted to targets with $\rho^2 > 0.90$, and the one on the right to targets with $\rho^2 > 0.98$. Compare the quality of the depth estimates for $\rho^2 > 0.98$ with the corresponding EM61 depths for $\rho^2 > 0.98$ in Figure 11. The magnetometer data appear to be more robust, yielding better depth estimates than EM61 data with comparable dipole fit quality.

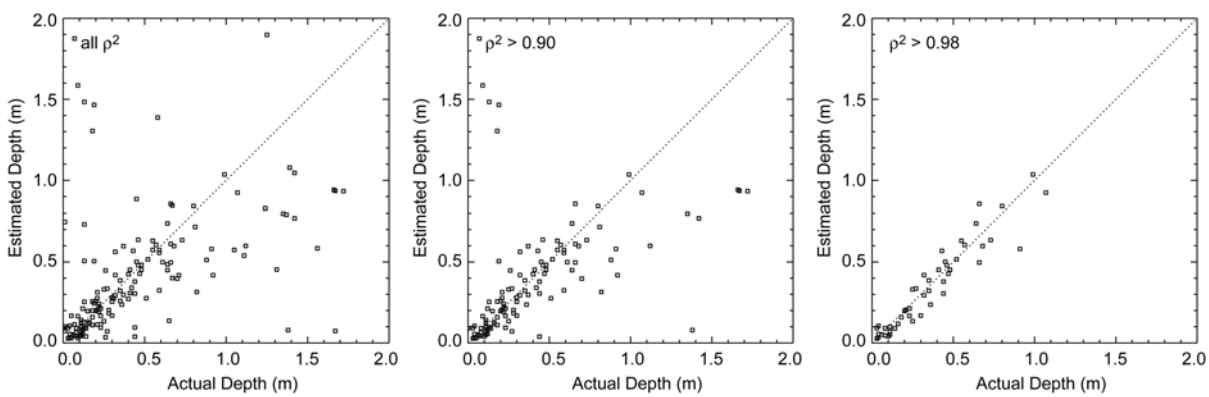

Figure 21. Target depth estimates from MTADS magnetometer array data compared with ground truth.

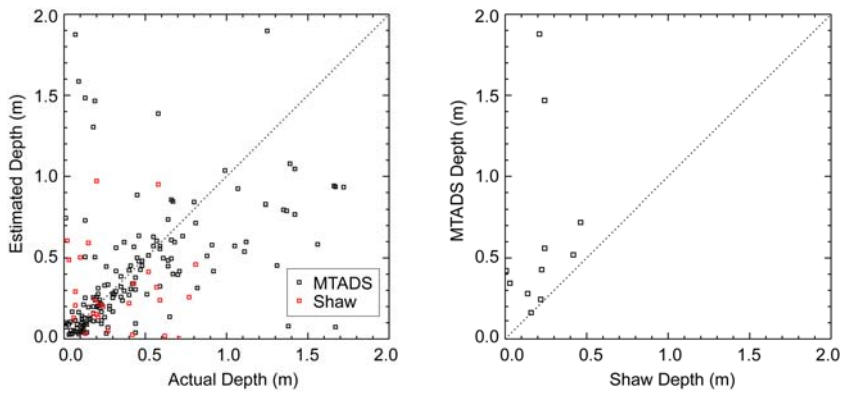

Figure 22. Comparison of estimated depths from MTADS and Shaw magnetometer data.

From Figure 19 it is apparent that most of the analyzed magnetic anomalies from the Shaw pushcart data had relatively low dipole fit quality. Indeed, the fit quality was greater than 0.90 for only four of the anomalies. Consequently, in comparing target depths estimated from the Shaw data with ground truth and with depths estimated from the MTADS data we use all targets regardless of fit quality. The results are shown in Figure 22. The plot on the left reproduces the leftmost plot from Figure 21, with corresponding results from the Shaw survey overplotted in red. The plot on the right is a direct comparison of depths estimated from the Shaw data with those from the MTADS data for common targets. The scatter in the left-hand plot is more or less the same for both data sets. Interestingly, the two outliers in the right-hand plot seem to represent bad depth estimates from the MTADS data rather than from the Shaw data. However, those points drop out from the MTADS results when $\rho^2 > 0.98$ (right-hand plot in Figure 21).

Corresponding results for target size estimates from magnetic dipole fits are shown in Figure 23. The plot on the left compares the MTADS dipole fit based size estimates with ground truth for the ordnance items. The results for $\rho^2 > 0.98$ are generally good. The RMS scatter in the estimated sizes relative to actual UXO caliber is comparable to the historical ±25% for these data. The plot on the right compares estimated sizes from the Shaw data with those from the MTADS data for common targets. The correlation between the two sets of results is good. The generally good performance for target size estimation with good ($\rho^2 > 0.98$) data is significant because, as noted previously, UXO/clutter discrimination based on target size can be quite useful at limited use sites.

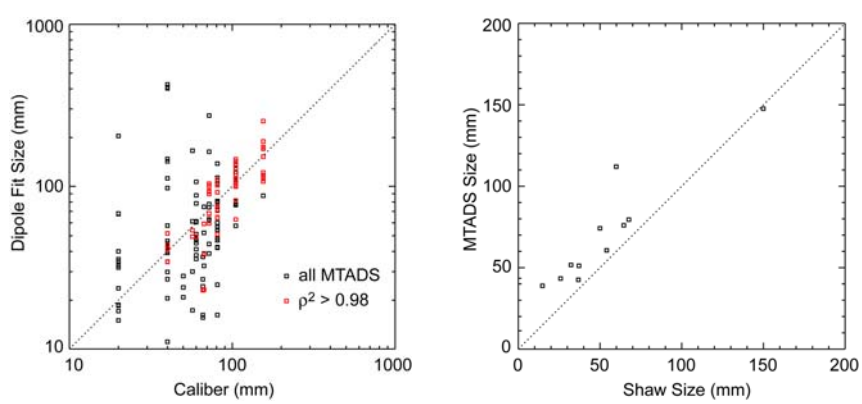

Figure 23. Dipole fit size estimates compared with ground truth for MTADS data (left) and comparison of Shaw and MTADS size estimates for common targets (right).

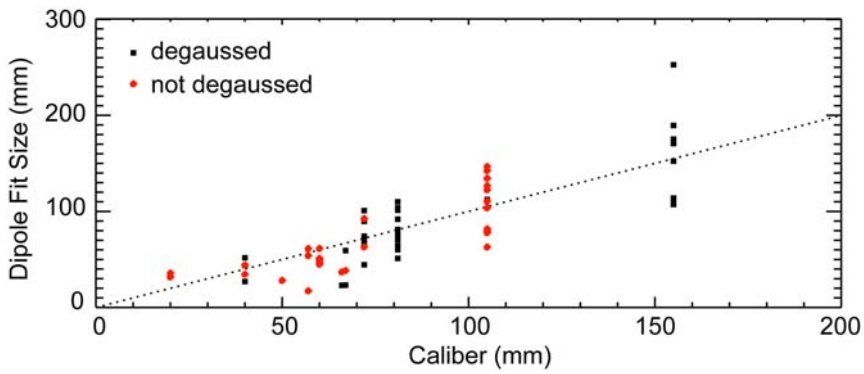

Figure 24. Comparison of dipole size estimates for degaussed and non-degaussed UXO targets.

4.3 Remnant Magnetization

Some of the targets at the standardized sites were degaussed prior to emplacement in order to erase any remnant magnetization. As noted at the beginning of this section, remnant magnetization can bias dipole size estimates because strong remnant magnetization can significantly bias a target's magnetic dipole moment. Figure 24 compares dipole size estimates for 33 degaussed and 33 non-degaussed UXO targets with reasonably good fit quality ($\rho^2 > 0.92$). Since there is little to distinguish between the two distributions, so it appears that degaussing did not significantly improve the accuracy of the target size estimates for these data.

5. Multiple Targets

Many real world UXO remediation sites contain highly contaminated regions with a high density of anomalies, both UXO and clutter. In these cases, where the signatures from multiple targets overlap the standard discrimination techniques will not work properly. That is because these techniques assume there is a single source whose signature is spatially separated from other signatures. Improvement might be made using standard techniques on multiple target signatures if there were some indication during the analysis that more than one target is present. Some of the cells of the Blind Grid at APG contained multiple targets. We have examined what happens when standard dipole fitting procedures are applied to such data in order to determine if that provides any ability to distinguish between single and multiple target anomalies.

Data collected with the TtFW EM61 sensor and the MTADS magnetometer array at the APG Blind Grid over the cells with more than one buried target were analyzed with the standard processing used for all other anomalies. Data from cells with only a single, isolated, target were also analyzed for comparison.

Figure 25 shows the dipole fit quality for both magnetometer (left) and EMI (right) data collected over double (red) and comparable single (black) targets at APG Blind Grid. It is clear that there is a wide range of dipole fit quality, and even the single targets cover approximately the same range of values. Presumably this is because the fit quality is not particularly good in general, and also because the fits for double targets are dominated by one or the other. In any event, the conclusion is that standard processing does not give a reliable indication of multiple targets..

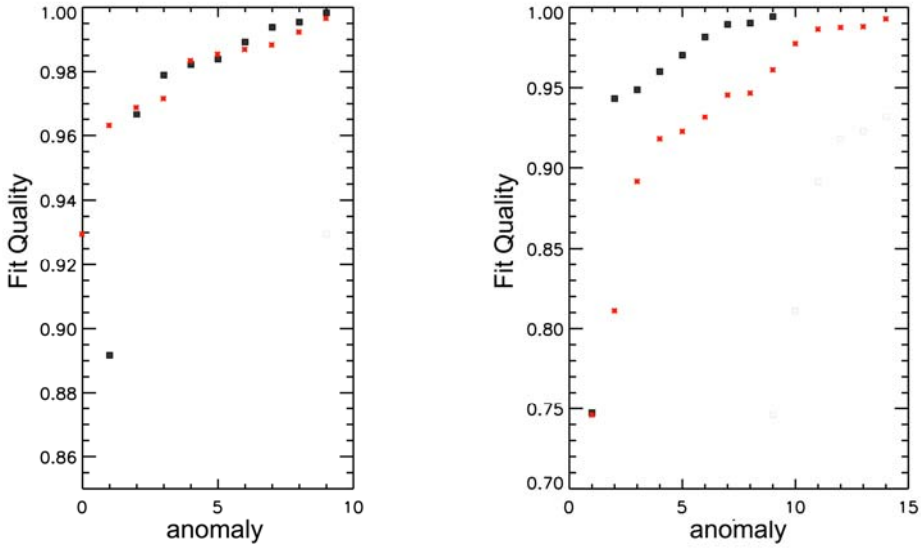

Figure 25. Fit quality distributions for multiple (red) and single (black) targets. MTADS magnetometer array data on left, TtFW EM61 data on right.

6. Summary and Conclusions

We have analyzed survey data collected by various demonstrators at the Standardized UXO Technology Demonstration Sites using the standard dipole response model wherein the magnetic or electromagnetic response of a target is represented by an induced dipole moment at the target location. Spatially mapped data collected over the target are inverted using this model to determine the target's location and depth and the parameters or features which characterize the target response. Performance metrics used in the analyses include target signal-to-noise-ratio (SNR), dipole fit quality (squared correlation between the data and the dipole model fit to the data) and the accuracy of target depth and target parameter estimates (size, polarizabilities) which are used for target classification and discrimination. With carefully collected data, dipole fit quality increases with target SNR in a predictable way, so comparisons of dipole fit quality and SNR help to establish if poor fits are due to weak signals and/or high noise levels or to data collection problems. Target characterization and discrimination is based on the target parameters or features determined from inversion of the data using the dipole response model. Dipole fit quality is generally the best indicator of the fidelity of the calculated target parameters.

Target depth estimates from EMI data generally improve with fit quality. Most of the estimated depths are within ±25 cm, but even with the targets restricted to fit quality greater than 0.98 there are significant outliers. There are also significant outliers in the corresponding target size estimates, generally corresponding to targets for which the depth was overestimated. However, for the bulk of the data the target size estimates vary with UXO caliber as predicted by theory. Some classification and discrimination on the basis of target size may be possible at limited use sites where the UXO have a narrow size range. However, given the overall data quality in the surveys analyzed here, shape-based discrimination is problematic. We believe that be basic problem is geolocation errors which effectively add a substantial noise component to the dipole inversion, significantly degrading the accuracy of the estimated target features.

Results from the magnetometer analysis show that very accurate depth estimates are obtained with data having fit quality greater than 0.98. For these data, the size estimates are consistent with historical data. Analysis of remnant magnetization based on a comparison of results from degaussed and non-degaussed UXO targets shows no significant differences between target parameter distributions for the two classes were observed.

Generally speaking the results are disappointing. Only a relatively small fraction of the survey data analyzed here is accurate enough to support reliable feature-based target classification and discrimination. Even when the target SNR is relatively high the dipole fit quality is frequently relatively poor, suggesting that the problems are due to deficiencies in the surveys, especially sensor location errors.

7. References

1. T. Bell, B. Barrow and N. Khadr, “Shape-Based Classification and Discrimination of Subsurface Objects Using Electromagnetic Induction,” International Geoscience and Remote Sensing Symposium (IGARSS’98), Seattle, Washington, July 6-10, 1998.
2. T. Bell, “Looking for a Perfect Match: Model-based Characterization Fits Data to UXO Signatures,” Ordnance and Explosives Environment 4(2), April-June 1997.
3. S. D. Billings, "Discrimination and classification of buried unexploded ordnance using magnetometry: IEEE Transactions of Geoscience and Remote Sensing," 42, pp. 1241-1251, 2004.
4. Thomas H. Bell, Bruce J. Barrow, and Jonathan T. Miller, "Subsurface Discrimination Using Electromagnetic Induction Sensors," IEEE Transactions on Geoscience and Remote Sensing, 39(6), pp. 1286-1293, June 2001.
5. B. Barrow, T. Bell, and N. Khadr, Evaluation of Laser Based Positioning for Characterization of EMI Signals from UXO. Proceedings of SAGEEP Conference, Seattle, Wash., April 2006.
6. L. D. Landau and E. M. Lifschitz, *Electrodynamics of Continuous Media*, Pergammon Press, New York, 1960, §§45, 62.
7. Peter. B. Weichman, "Surface Modes and Multipower-Law Structure in the Early-Time Electromagnetic Response of Magnetic Targets," Physical Review Letters, 93(2), 023902, 9 July 2004.
8. J. Torquil Smith, H. Frank Morrison and Alex Becker, "Parametric Forms and the Inductive Response of a Permeable Conducting Sphere," J. Environmental and Engineering Geophysics, 9(4), pp. 213-216, December 2004.
9. B. Barrow and H. H. Nelson, "Effects of Positioning Error on Inverting EMI Data for UXO Discrimination using the MTADS Platform," UXO/Countermine Forum, New Orleans, April 9-12, 2001.
10. B. Barrow and H.H. Nelson, "EMI Signatures from Large Projectiles and Exploded Projectile Fragments on a Seeded Live Site," UXO/Countermine Forum, Orlando, September 2002.
11. Thomas Bell, “Geolocation Requirements for UXO Discrimination,” presented at the SERDP/ESTCP Geolocation Workshop, June 1-2, 2005.
12. T. Bell, D. DeProspo and M. Prouty, “MagAID: PC-Based Target Characterization Software for use with Total Field Magnetometer Survey Data,” 9th Symposium on the Application of Geophysics to Environmental and Engineering Problems (SAGEEP), Keystone Conference Center, Colorado, April 28-May 1, 1996; Conference Proceedings pp.639-647.